

# Imaging *ex vivo* and *in vitro* brain morphology in animal models with ultrahigh resolution optical coherence tomography

**Kostadinka Bizheva**  
**Angelika Unterhuber**  
**Boris Hermann**  
**Boris Považay**  
**Harald Sattmann**  
**Wolfgang Drexler**

Department of Medical Physics,  
Medical University of Vienna  
and Christian Doppler Laboratory,  
Vienna A-1090, Austria

**Andreas Stingl**  
**Tuan Le**

FEMTOLASERS GmbH,  
Fernkorngasse 10,  
Vienna A-1010, Austria

**Michael Mei**  
**Ronald Holzwarth**

MenloSystems GmbH,  
D-80799 Munchen, Germany

**Herbert A. Reitsamer**

Department of Physiology,  
Medical University of Vienna,  
Vienna A-1090, Austria

**John E. Morgan**  
**Alan Cowey**

University Hospital of Wales Health Park,  
Cardiff, Wales,  
United Kingdom

**Abstract.** The feasibility of ultrahigh resolution optical coherence tomography (UHR OCT) to image *ex vivo* and *in vitro* brain tissue morphology on a scale from single neuron cells to a whole animal brain was investigated using a number of animal models. Sub-2- $\mu\text{m}$  axial resolution OCT in biological tissue was achieved at different central wavelengths by separately interfacing two state-of-the-art broad bandwidth light sources (titanium:sapphire, Ti:Al<sub>2</sub>O<sub>3</sub> laser,  $\lambda_c = 800$  nm,  $\Delta\lambda = 260$  nm,  $P_{\text{out}} = 50$  mW and a fiber laser light source,  $\lambda_c = 1350$  nm,  $\Delta\lambda = 470$  nm,  $P_{\text{out}} = 4$  mW) to free-space or fiber-based OCT systems, designed for optimal performance in the appropriate wavelength regions. The ability of sub-2- $\mu\text{m}$  axial resolution OCT to visualize intracellular morphology was demonstrated by imaging living ganglion cells in cultures. The feasibility of UHR OCT to image the globular structure of an entire animal brain as well as to resolve fine morphological features at various depths in it was tested by imaging a fixed honeybee brain. Possible degradation of OCT axial resolution with depth in optically dense brain tissue was examined by depositing microspheres through the blood stream to various depths in the brain of a living rabbit. It was determined that in the 1100 to 1600-nm wavelength range, OCT axial resolution was well preserved, even at depths greater than 500  $\mu\text{m}$ , and permitted distinct visualization of microspheres 15  $\mu\text{m}$  in diameter. In addition, the OCT image penetration depth and the scattering properties of gray and white brain matter were evaluated in tissue samples from the visual cortex of a fixed monkey brain. © 2004 American Institute of Physics.  
[DOI: 10.1117/1.1756920]

Keywords: optical coherence tomography; biomedical optics; medical imaging; brain imaging.

Paper 03114 received Sep. 17, 2003; revised manuscript received Dec. 1, 2003; accepted for publication Dec. 5, 2003.

## 1 Introduction

In recent years there has been a constant demand for development of noninvasive or minimally invasive imaging techniques that can be applied in neurosurgery as guiding tools and as an alternative to standard excisional biopsy. So far a vast variety of imaging methods<sup>1–4</sup> ranging from magnetic resonance imaging (MRI) to optical microscopy have been used at different stages in the diagnostics, treatment, and post-operative monitoring of various neuropathologies. Despite all their advantages, each of these methods possesses some inherent limitation related to image resolution, acquisition time, specificity and accuracy of the acquired image or information, etc., which motivates the constant search for new more precise and less invasive imaging modalities.

In neurosurgery the goal of any intracranial intervention is to provide accurate localization, diagnosis, and appropriate treatment of intracranial abnormalities, while causing minimal

damage to the intact brain. During open skull surgery, the boundaries of some lesions, in particular low-grade gliomas, as well as the presence and location of small metastases of various brain tumors, may be difficult to determine by visual inspection or microscopic imaging of the tissue surface. Since brain pathologies are characterized by alterations in the morphology and physiology of healthy brain tissue, an imaging method with sufficient resolution and penetration depth that is able to discriminate between healthy and pathological brain tissue can find applications in neurosurgery as a diagnostics tool.

Optical coherence tomography (OCT) is a noncontact optical imaging method that combines micrometer-scale resolution with millimeter image penetration depth<sup>5–7</sup> and as such may have a potential as a guiding and diagnostics tool in neurosurgery. Although OCT has been successfully applied to many biomedical fields, such as ophthalmology, dermatology, gastroenterology, etc.<sup>8</sup> since its invention about a decade ago, so far only a few attempts have been made to image brain

Address all correspondence to Dr. Wolfgang Drexler, University of Vienna, Waehring Strasse 13, Vienna A-1090, Austria. Tel: +43 1 4277 60726; Fax: +43 1 4277 9607; E-mail: Wolfgang.Drexle@univie.ac.at

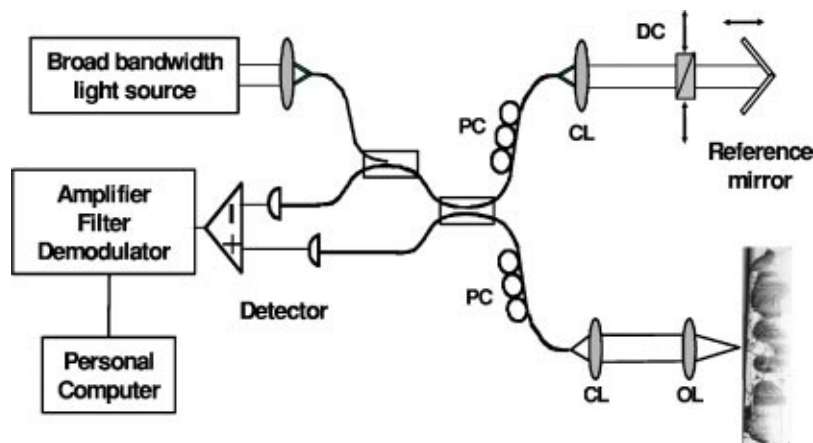


**Fig. 1** Schematic of a fiber-based UHR OCT system: CL, collimating lens; OL, objective lens; DC, dispersion compensation unit; PC, polarization controllers.

tissue morphology and function with standard resolution OCT.<sup>9–12</sup> However, the spatial resolution in these cases (axial resolution  $\sim 10$  to  $15 \mu\text{m}$ ) was insufficient to permit visualization of fine morphological details such as microcalcifications and displasias that are characteristic of various types of brain tumors. Recent advances in laser technology have led to the development of UHR OCT,<sup>13–19</sup> (axial resolution  $< 2 \mu\text{m}$ ), and current research in ophthalmology has clearly demonstrated the feasibility of UHR OCT to image intraretinal morphology, as well as to view small structural features in intraocular pathologies.<sup>20–22</sup>

The objective of this project was to investigate the feasibility of using UHR OCT to visualize small morphological features in brain tissue by using animal models and to establish a correlation between structural details present both in the OCT tomograms and in the eosin-stained histological cross-sections. In addition, this study aimed to determine the wavelength region in which UHR OCT in optically dense brain tissue can provide optimal image contrast and depth penetration, as well as to explore the degradation of OCT axial resolution with depth in biological tissue.

## 2 Methods

Sub- $2\text{-}\mu\text{m}$  axial OCT resolution in biological tissue was achieved by using two broad bandwidth light sources: a state-of-the-art, prismless titanium:sapphire ( $\text{Ti}:\text{Al}_2\text{O}_3$ ) laser<sup>23</sup> ( $\lambda_c = 800 \text{ nm}$ ,  $\Delta\lambda = 260 \text{ nm}$ , and  $P_{\text{out}} = 50 \text{ mW}$ ), and a novel, fiber laser-based light source<sup>24</sup> (MenloSystems,  $\lambda_c = 1350 \text{ nm}$ ,  $\Delta\lambda = 470 \text{ nm}$ , and  $P_{\text{out}} = 4 \text{ mW}$ ). The two light sources were interfaced alternatively to either a free-space OCT system (described in detail in Ref. 24) or to appropriate fiber-based OCT systems specifically designed to operate in the 600 to 1000-nm and 900 to 1500-nm wavelength ranges (Fig. 1). All optical and fiber optic components were selected to support the propagation of broadband light through the systems with minimal spectral and power losses, as well as to compensate for any polarization and dispersion mismatch between the sample and reference arm of the interferometers. Dynamic focusing was implemented in the free-space OCT system to prevent loss of spatial resolution resulting from defocusing, while in the fiber-based OCT systems, the same

effect was compensated for by acquiring and subsequently fusing multiple tomograms obtained at different depths at the same transverse location. The image acquisition rates for the free-space and the fiber-based OCT systems were 10 A-scans/s and 250 A-scans/s, respectively. The OCT systems were evaluated to provide  $0.9 \times 2 \mu\text{m}$  (axial  $\times$  lateral) resolution in biological tissue, and a sensitivity of 110 dB for 5 mW at the sample surface for the case of the  $\text{Ti}:\text{Al}_2\text{O}_3$  laser ( $\lambda_c = 800 \text{ nm}$ ) and  $1.4 \times 4.5 \mu\text{m}$  spatial resolution and 98 dB sensitivity at 0.5 mW for the case of the MenloSystems fiber laser-based light source ( $\lambda_c = 1350 \text{ nm}$ ). Full fringe detection was realized by use of a high-speed (10 Ms/s), 16-bit A/D converter to digitize the fringe data, thus permitting extraction of functional and spectroscopic information in addition to the high-resolution morphological imaging.

For the purpose of this study, tissue samples were prepared from the brains of honeybees, rabbits, and monkeys. The sophisticated structural organization of the honeybee brain, along with its small size, have made it an ideal object for testing the ability of UHR OCT to image small morphological details and to discriminate among tissue layers in optically dense brain tissue. The monkey brain was chosen because its structural organization and tissue optical properties most closely resemble the human brain. To test the ability of UHR OCT to image subcellular features in living neuronal cells, cell cultures of sympathetic ganglion cells were obtained from rat superior cervical ganglia.

Because postmortem brain tissue quickly loses optical quality as a result of cell degradation, all brain tissue samples were fixed in 4% paraformaldehyde solution. Depending on the animal model, a brain tissue slice or the whole brain was placed in a custom-designed chamber with an optical window ( $\sim 150 \mu\text{m}$  thick glass coverslip) through which the tissue was imaged. During the imaging procedure, care was taken to properly compensate for the dispersion mismatch introduced by the glass coverslip and the excess fixation solution between the glass window and the tissue surface in order to preserve the high OCT axial resolution in all imaged tissue samples.

For the case of the honeybee, eosin-stained histological cross-sections ( $5 \mu\text{m}$  thick) of the whole brain were prepared

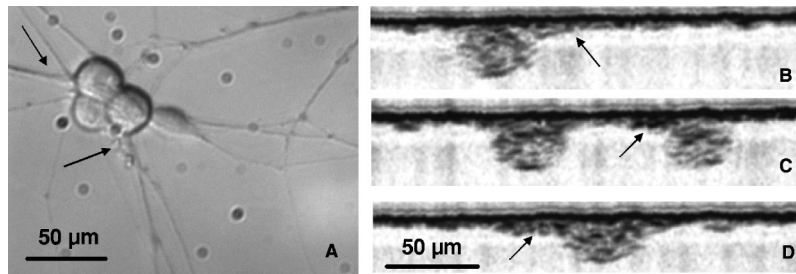


**Fig. 2** A microscope image of living ganglion cells (a) compared with UHR OCT tomograms of the cells acquired at  $\lambda_c \sim 800$  nm with 110-dB sensitivity (b) to (d). The highly reflective (black) spots in the OCT images most likely correspond to optically dense cell nuclei and organelles, while the pale gray area around them corresponds to the cell cytoplasm. The black arrows mark possible axonal extensions of the ganglion cells.

and imaged with a regular microscope for comparison with the OCT tomograms. To examine the degradation of OCT axial resolution with imaging depth in optically dense brain tissue, resulting from dispersion mismatch and detection of multiply scattered light,  $15\text{-}\mu\text{m}$  large microspheres were injected into the blood stream of a living rabbit. After euthanasia, the rabbit brain was fixed in 4% paraformaldehyde and cross-sections containing microspheres trapped in small blood vessels were identified using a regular microscope. Tissue slices were also obtained from the visual cortex of a fixed monkey brain. For the case of imaging cell morphology, ganglion cell cultures were prepared on protein-coated glass coverslips and placed in a custom-designed perfusion chamber filled with nutritious solution to preserve the normal condition of the cells.

### 3 Results and Discussion

To test the suitability of UHR OCT for imaging morphology of neuron cells, a series of images were obtained from ganglion cell cultures using the fiber-based OCT system. Figures 2(b) to 2(d) show tomograms of single cells and groups of cells acquired at  $\lambda_c \sim 800$  nm with 110-dB sensitivity compared with a representative image of the cells obtained with a regular microscope [Fig. 2(a)]. Considering the average size of the cells ( $<50\ \mu\text{m}$ ) and the depth of focus of the imaging optics ( $\sim 80\ \mu\text{m}$ ), the imaging beam was focused slightly below the glass/solution interface and single tomograms of the cells were acquired (no fusing of images acquired at different focal depths was necessary). The thick black line in the upper part of all OCT images corresponds to a reflection from the glass coverslip, to which the cells were attached. The highly reflective (black) spots most likely correspond to various cell organelles, judging from the high optical density and the size of the objects. Although the cell membrane is not clearly visualized, the boundaries of the cell cytoplasm (pale gray color) are distinctly visible. Furthermore, the high spatial OCT resolution permits imaging of the thin axonal extensions of the ganglion cells (marked with black arrows in Fig. 2). Previous research on isolated neurons has demonstrated that the propagation of action potentials is accompanied by cell membrane depolarization, which further results in changes in the light-scattering properties of the cell, which are most pronounced at the base of the axon.<sup>25</sup> Distinct visualization of neuronal axonal extensions in cell cultures containing multiple cells may provide useful information on the transmission of signals in neuronal networks.

To examine the feasibility of UHR OCT for imaging fine morphological details in depth in optically dense brain tissue, tomograms were acquired from the fixed whole brain of a honeybee. Figure 3(a) shows a schematic of the bee brain, where the dotted white line marks the location of a representative OCT tomogram. Although the bee brain is very small ( $\sim 1\ \text{mm}^3$ ), it has a sophisticated globular structure and functional organization that correspond to a vast repertoire of behavioral patterns.<sup>26–28</sup> Furthermore, neurons in the bee brain

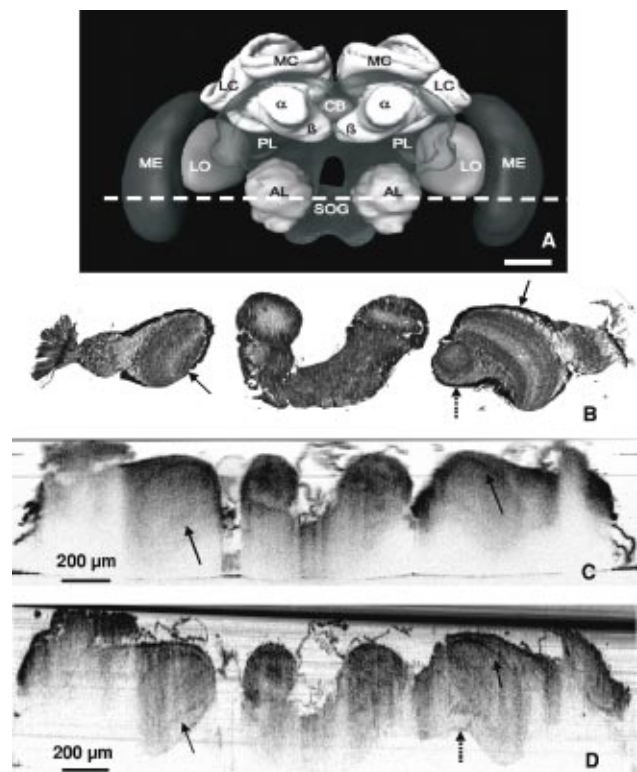


**Fig. 3** (a) Schematic representation of the honeybee brain: MC, medial calyx; LC, lateral calyx; CB, cerebral bridge; LO, lobula; ME, medulla; PL, lobula plate; AL, antenna lobes; SOG, suboesophageal ganglion,  $\alpha$ - and  $\beta$ -lobes. (b) A stained histological cross-section. (c) An OCT tomogram acquired with a resolution of  $\sim 3 \times 1.4\ \mu\text{m}$  (lateral  $\times$  axial) and 110-dB sensitivity for 8-mW incident power. (d) An OCT tomogram acquired with a resolution of  $\sim 4.5 \times 1.4\ \mu\text{m}$  and 98-dB sensitivity for 500- $\mu\text{W}$  incident power. Image dimensions:  $3 \times 1\ \text{mm}$  ( $6000 \times 2000$  pixels). Solid black arrows mark boundaries of various tissue layers, while the dotted black arrow point at the lobula.

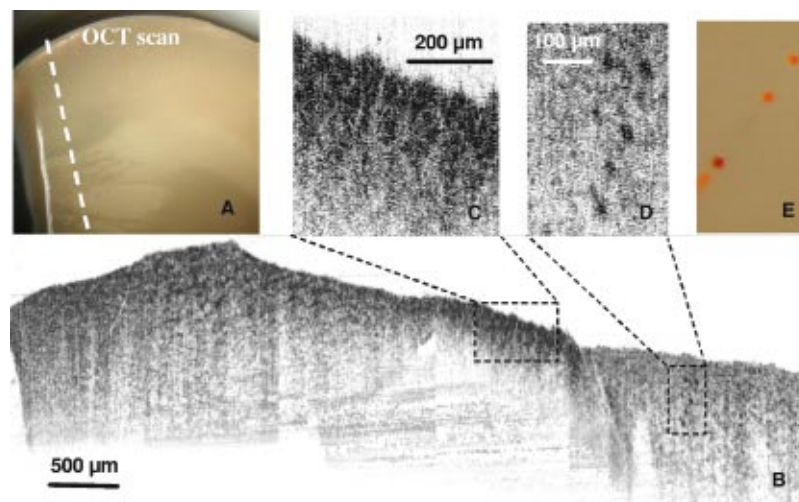


**Fig. 4** (a) A microscope image of a rabbit brain slice in which the white dashed line marks the location of a transverse OCT scan. (b) Corresponding OCT tomogram ( $6 \times 2$  mm) acquired at  $\lambda_c \sim 1350$  nm with 98-dB sensitivity. Insets: (c) enlarged view of the nerve fiber bundles, (d) enlarged view of the embedded microspheres, and (e) a regular microscope image of the microspheres.

are spatially organized to form layers for example, the visual center of the brain [medulla, Fig. 3(a), ME] contains alternating layers composed of neuron somas and axonal extensions, while the neurons in the antenna lobes [Fig. 3(a), AL] are oriented in such a way that the somas create a spherical shell inside which the axonal extensions are tightly packed. Approximately 20 OCT tomograms ( $3 \times 1$  mm), separated by steps of  $25 \mu\text{m}$  were obtained from the bee brain with both the  $\text{Ti:Al}_2\text{O}_3$  laser (coupled to the fiber-based OCT system) and the fiber-based light source (interfaced to the free-space OCT system). Figure 3 shows representative images acquired at  $\lambda_c \sim 800$  nm [Fig. 3(c)] and  $\lambda_c \sim 1350$  nm [Fig. 3(d)] through the medulla and the antenna lobes at a location marked with a dotted white line in Fig. 3(a). Since the fiber-based OCT system has a limited depth of focus, to minimize loss of transverse image resolution, three tomograms were acquired at different focal depths and fused together to produce the image in Fig. 3(c). Figure 3(b) shows the corresponding histological cross-section. Boundaries between different cell layers are distinctly outlined on both OCT tomograms (marked with solid black arrows) and correspond well to the layered structure observed in the histological image. A part of the lobula [Fig. 3(a), LO] positioned below the medulla is clearly visible on the right side of the image acquired at longer wavelengths [Fig. 3(d), dotted black arrow] and corresponds well to the structure observed in the histological cross-section. Note that the central parts of the antenna lobes appear dark (highly backscattering), surrounded by a ring of low backscattering tissue. This appearance can be explained by the fact that the large number of tightly packed axon-dendritic cell extensions tend to scatter light more than the neuron somas. Additional OCT tomograms acquired at various locations in the bee brain and not shown here also demonstrated the ability of UHR OCT to clearly visualize the nerve fiber bundles connecting the medulla with the honeybee eyes, as well as the honeycomb structure of the bee's eyes consisting of small compartments  $30$  to  $50 \mu\text{m}$  in diameter. Although the tomogram in Fig. 3(d) obtained with the fiber-based light source was acquired with significantly lower sen-

sitivity (98 dB versus 105 dB for  $\text{Ti:Al}_2\text{O}_3$ ), the penetration depth and the overall image quality were comparable to that of the tomogram acquired with the  $\text{Ti:Al}_2\text{O}_3$  laser. In general, light scattering in optically dense tissue decreases monotonically with wavelength,<sup>29</sup> which accounts for the better image penetration in all tomograms acquired at  $\lambda_c \sim 1350$  nm compared with images obtained at  $\lambda_c \sim 800$  nm.

Figure 4 summarizes representative results from the test of OCT axial resolution degradation in brain tissue. Figure 4(a) shows a regular microscope image of a fixed rabbit brain slice. The white dashed line through it marks the position of a transverse OCT scan acquired through the gray and white brain matter using the fiber-based light source coupled to the free-space OCT system. Figure 4(b) shows the OCT image ( $6 \times 2$  mm), the left edge of which corresponds to the brain surface. The tomogram clearly demonstrates the difference in optical scattering properties of gray and white brain matter, resulting in varying image depth penetrations through the tomogram. The penetration depth is approximately 1 mm in gray matter (left part of the image) and diminishes to less than  $500 \mu\text{m}$  in white matter (close to the central part of the image). The OCT scan was acquired at a location near the brainstem where nerve fiber bundles are abundant. The central part of the OCT tomogram shows a group of densely packed, almost elliptically shaped nerve fiber bundles. Figure 4(c) presents an enlarged view of the region and demonstrates the ability of UHR OCT to distinctly outline single fiber bundles  $\sim 50 \mu\text{m}$  in size in a transverse direction.

The right part of the OCT tomogram shows a number of highly reflective (dark) spots, almost spherical in shape and positioned on a straight line [Fig. 4(c), enlarged view of the region]. A comparison with regular microscope images [Fig. 4(e)] revealed that the spots correspond to  $15\text{-}\mu\text{m}$ -diameter microspheres embedded in a small blood vessel. Considering that both water dispersion<sup>30,31</sup> and detection of multiply scattered light<sup>32</sup> can cause degradation of OCT image axial resolution as a function of depth in biological tissue, it is important to note that in this case the deterioration of image reso-

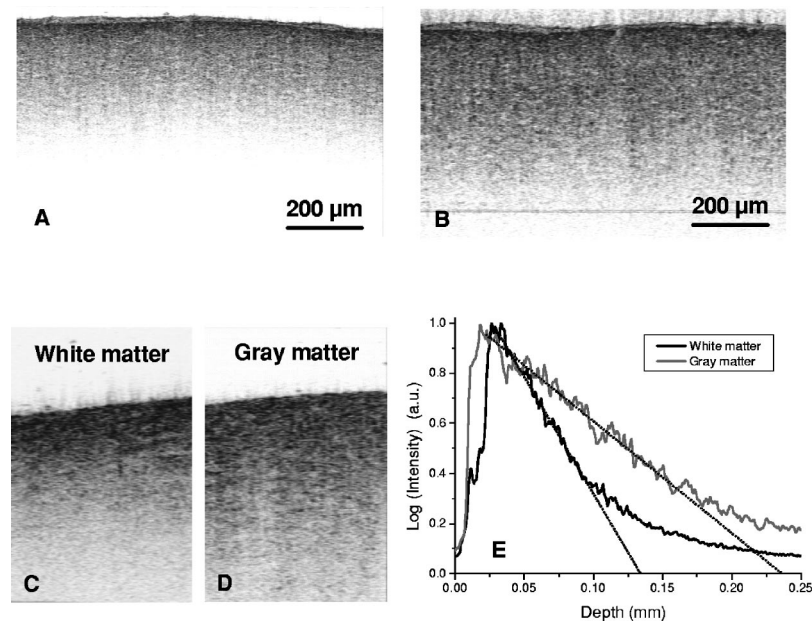


**Fig. 5** (a) OCT tomograms of a monkey visual cortex ( $1 \times 0.62$  mm) acquired at  $\lambda_c \sim 800$  nm with 110-dB sensitivity and (b) at  $\lambda_c \sim 1350$  nm with 98-dB sensitivity. (c) OCT tomograms of gray and (d) white brain matter and (e) plot of the corresponding reflectivity profiles as functions of imaging depth extracted from a transverse OCT image by averaging over twenty adjacent A-scans.

lution was not sufficient to prevent distinct visualization of a 15- $\mu\text{m}$  large microsphere positioned at a depth of  $\sim 500$   $\mu\text{m}$  below the brain tissue surface.

To evaluate the OCT image penetration depth in fixed brain tissue, tomograms were obtained from a brain slice from the visual cortex of a monkey brain with both the Ti:Al<sub>2</sub>O<sub>3</sub> laser and the fiber-based laser. Figure 5 shows two representative OCT images ( $1 \times 0.63$  mm) acquired at  $\lambda_c \sim 800$  nm with 110-dB sensitivity [Fig. 5(a)] and at  $\lambda_c \sim 1350$  nm with 98-dB sensitivity [Fig. 5(b)]. In both tomograms the brain tissue appears almost homogeneous, with no distinct layered structure, except for the clearly visualized dura. In general, the monkey visual cortex (thickness  $\sim 0.5$  mm) consists of six layers characterized by different thicknesses, cell types, and cell densities. The lack of a distinctly visible layered structure in the OCT tomograms may be caused by two factors: first, the spatial distribution and density of neuron somas varies slowly and gradually from one layer to the next, so the layers' boundaries are not distinctly outlined; and second, the fixation in 4% paraformaldehyde changes the optical properties of brain tissue and may reduce the naturally existing contrast between neuron somas and the extracellular milieu.

To determine the scattering properties of fixed brain matter in the 670 to 930-nm wavelength range, OCT tomograms of gray and white brain matter were acquired [Figs. 5(c) and 5(d)]. Reflectivity profiles as functions of imaging depth were extracted by averaging over twenty adjacent A-scans [Fig. 5(e)]. The scattering coefficient averaged over the spectral bandwidth of the Ti:Al<sub>2</sub>O<sub>3</sub> laser was evaluated to be  $\mu_s \sim 9$   $\text{mm}^{-1}$  in the case of gray matter, which compared well with previously published data on the optical properties of human brain tissue.<sup>33</sup> However, for white matter, the measured scattering coefficient  $\mu_s \sim 22$   $\text{mm}^{-1}$  was about 30% smaller relative to the value obtained for fresh human white matter. This discrepancy may be attributed to two factors. It is

possible that monkey white brain matter is not as highly scattering as human white matter, or that the difference arises from the fixation of the monkey brain in 4% formaldehyde. Since neither fresh monkey brain slices nor literature values for the scattering properties of fresh monkey white matter were available during this study, this discrepancy remains to be investigated in the future.

## 4 Conclusion

The feasibility of UHR OCT for imaging *in vitro* brain tissue morphology on the scale from single neuron cells to the structural organization of an entire animal brain was investigated with the intention of determining the suitability of this imaging technique as a potential diagnostics and research tool in neurology and neurosurgery. The results presented in this paper have demonstrated that although the UHR OCT penetration depth is limited to about 1 to 2 mm in optically dense brain tissue, the micrometer-scale image resolution is well preserved, even at greater imaging depths, to permit clear visualization of morphological features the size of 10 to 50  $\mu\text{m}$ . Furthermore, tomograms acquired in various animal brain tissue samples have shown that in cases when the neuron cell density and spatial distribution are such as to provide sufficient optical contrast, UHR OCT is able to spatially resolve layered or globular structures within the highly scattering brain matter. Considering that development of any neurological disease is accompanied by morphological and physiological changes on the cellular level or a larger scale, UHR OCT may be able to discriminate, not only between healthy and pathological brain tissue, but also between various neuro pathologies. Provided that future investigations confirm this hypothesis, UHR OCT may be successfully used as a diagnostics tool in neurology and neurosurgery.

In addition, the sub-2- $\mu\text{m}$  OCT axial resolution proved sufficient to distinguish intracellular components such as nuclei in cultures of living electrically active ganglion cells, as well as to image thin axonal cell extensions. These results are of significant importance, suggesting that UHR OCT may find applications as an investigative technique in basic neurological research.

### Acknowledgments

The authors gratefully acknowledge contributions from S. Huck (Brain Research Institute, Vienna University Medical School), Michael Kempe and Bernhard Zimmermann (Carl Zeiss Jena GmbH, Germany), L. Schachinger (Dept. of Medical Physics, University of Vienna), S. Strommer (Dept. of Dermatology, University of Vienna), H. Huemer and C. Schubert (Dept. of Physiology, University of Vienna). This research has been financially supported by FEMTOLASERS GmbH, Christian Doppler Laboratory and by the following grants: FWF P14218-PSY, FWF Y 159-PAT, CRAF-1999-70549.

### References

- J. Hoffman, "New advances in brain tumor imaging," *Curr. Opin. Oncol.* **13**, 148–153 (2001).
- R. Acharya, R. Wasserman, J. Stevens, and C. Hinojosa, "Biomedical imaging modalities: a tutorial," *Comput. Med. Imaging Graph.* **19**, 3–25 (1995).
- N. A. Sharif and M. E. Lewis, Eds., *Brain Imaging*, Ellis Horwood Ltd., London (1989).
- R. Frostig and M. A. L. Nicolelis, Eds., *In Vivo Optical Imaging of Brain Function*, CRC Press, Boca Raton, FL (2002).
- D. Huang, E. A. Swanson, C. P. Lin, J. S. Schuman, W. G. Stinson, W. Chang, M. R. Hee, T. Flotte, K. Gregory, C. A. Puliafito, and J. G. Fujimoto, "Optical coherence tomography," *Science* **254**, 1178–1181 (1991).
- J. G. Fujimoto, M. Brezinski, G. Tearney, S. A. Boppart, B. Bouma, M. Hee, J. Southern, and E. Swanson, *Nat. Med.* **1**, 970–972 (1995).
- A. F. Fercher, "Optical coherence tomography," *J. Biomed. Opt.* **1**, 157–173 (1996).
- B. Bouma and J. Tearney, Eds., *Handbook of Optical Coherence Tomography*, Marcel Dekker, New York (2002).
- S. A. Boppart, M. Brezinski, C. Pitris, and J. G. Fujimoto, "Optical coherence tomography for neurosurgical imaging of human intracortical melanoma," *Neurosurgery* **43**, 834–841 (1998).
- R. Uma Maheswari, H. Takaoka, R. Homma, H. Kadono, and M. Tanifuji, "Implementation of optical coherence tomography (OCT) in visualization of functional structures of cat visual cortex," *Opt. Commun.* **202**, 47–54 (2002).
- M. Lazebnik, D. L. Marks, K. Potgieter, R. Gillette, and S. A. Boppart, "Functional optical coherence tomography for detecting neural activity through scattering changes," *Opt. Lett.* **28**, 1218–1220 (2003).
- S. Roper, M. D. Morgner, G. V. Gelikonov, F. I. Feldchtein, N. M. Beach, M. A. King, V. M. Gelikonov, A. M. Sergeev, and D. H. Reitze, "In-vivo detection of experimentally induced cortical dygenesis abnormality in the adult rat neocortex using optical coherence tomography," *J. Neurosci. Methods* **80**, 91–98 (1998).
- W. Drexler, U. Morgner, F. X. Kärtner, C. Pitris, S. A. Boppart, X. D. Li, E. P. Ippen, and J. G. Fujimoto, "In-vivo ultrahigh resolution optical coherence tomography," *Opt. Lett.* **24**, 1221–1223 (1999).
- I. Hartl, X. D. Li, C. Chudoba, R. K. Ghanta, T. H. Ko, J. G. Fujimoto, J. K. Ranka, and R. S. Windeler, "Ultrahigh resolution optical coherence tomography using continuum generation in an air-silica microstructure optical fiber," *Opt. Lett.* **26**, 608–610 (2001).
- B. Povazay, K. Bizheva, A. Unterhuber, B. Herman, H. Sattmann, A. Fercher, W. Drexler, A. Apolonski, W. J. Wadsworth, J. C. Knight, P. St. J. Russel, M. Vetterlein, and E. Scherzer, "Sub-micrometer resolution optical coherence tomography," *Opt. Lett.* **27**, 1800–1824 (2002).
- L. Vabre, A. Dubois, and A. C. Boccara, "Thermal light full-field optical coherence tomography," *Opt. Lett.* **27**, 530–532 (2002).
- K. Bizheva, B. Povazay, B. Hermann, H. Sattmann, W. Drexler, M. Mei, R. Holzwarth, T. Hoelzenbein, V. Wacheck, and H. Pehamberger, "Compact, broad bandwidth fiber laser for sub-2  $\mu\text{m}$  axial resolution optical coherence tomography in the 1300 nm wavelength region," *Opt. Lett.* **28**, 707–709 (2003).
- A. Unterhuber, B. Povazay, B. Hermann, H. Sattmann, V. Yakovlev, G. Tempea, C. Schubert, E. M. Anger, P. K. Ahnelt, M. Stur, J. E. Morgan, A. Cowey, G. Jung, T. Le, A. Stingl, and W. Drexler, "Compact low-cost Ti:Al<sub>2</sub>O<sub>3</sub> laser for in-vivo ultrahigh-resolution optical coherence tomography," *Opt. Lett.* **28**, 905–907 (2003).
- W. Drexler, "Ultrahigh resolution optical coherence tomography," *J. Biomed. Opt.* **9**, 47–74 (2004).
- W. Drexler, U. Morgner, R. K. Ghanta, J. S. Schuman, F. Kärtner, and J. G. Fujimoto, "Ultrahigh-resolution ophthalmic optical coherence tomography," *Nat. Med.* **7**, 502–507 (2001).
- M. Gloesmann, B. Hermann, C. Schubert, H. Sattmann, P. K. Ahnelt, and W. Drexler, "Histologic correlation of pig retina radial stratification with ultrahigh-resolution optical coherence tomography," *Invest. Ophthalmol. Visual Sci.* **44**, 1696–1703 (2003).
- W. Drexler, H. Sattmann, B. Hermann, T. K. Ko, M. Stur, A. Unterhuber, C. Scholda, O. Findl, M. Wirtitsch, J. G. Fujimoto, and A. F. Fercher, "Enhanced visualization of macular pathology with the use of ultrahigh-resolution optical coherence tomography," *Arch. Ophthalmol. (Chicago)* **121**, 695–706 (2003).
- T. Fuji, A. Unterhuber, V. S. Yakovlev, G. Tempea, F. Krausz, and W. Drexler, "Generation of smooth, ultra-broadband spectra directly from a prism-less Ti:sapphire laser," *Appl. Phys. B: Lasers Opt.* **77**, 125–128 (2003).
- K. Bizheva, B. Povazay, B. Herman, H. Sattmann, W. Drexler, M. Mei, R. Holzwarth, T. Hoelzenbein, V. Wacheck, and H. Pehamberger, "Compact, broad bandwidth fiber laser for sub-2  $\mu\text{m}$  axial resolution optical coherence tomography in the 1300 nm wavelength region," *Opt. Lett.* **28**, 1–3 (2003).
- R. A. Stepanoski, A. LaPorta, F. Raccuia-Behling, G. E. Blonder, R. E. Slusher, and D. Kleinfeld, "Non-invasive detection of changes in membrane potential in cultured neurons by light scattering," *Proc. Natl. Acad. Sci. U.S.A.* **88**, 9382–9386 (1991).
- R. E. Snodgrass, *Anatomy of the Honeybee*, Comstock Publishing Associates, Ithaca, NY (1956).
- M. L. Winston, *The Biology of the Honeybee*, Harvard University Press, Cambridge, MA (1987).
- R. Menzel and M. Giurfa, "Cognitive architecture of a min-brain: the honeybee," *Trends Cognit. Sci.* **5**, 62–71 (2001).
- J. M. Schmitt and G. Kumar, "Optical scattering properties of soft tissues: a discrete particle model," *Appl. Opt.* **37**, 2788–2797 (1998).
- W. Drexler, C. Hitzinger, A. Baumgartner, O. Findl, H. Sattmann, and A. F. Fercher, "Investigation of dispersion effects on ocular media by multiple wavelength partial coherence interferometry," *Exp. Eye Res.* **66**, 25–33 (1998).
- Y. Wang, J. Nelson, Z. Chen, B. Reiser, R. S. Chuck, and R. S. Windeler, "Optimal wavelength for ultra-high resolution optical coherence tomography," *Opt. Express* **11**, 1411–1417 (2003).
- K. Bizheva, A. K. Dunn, A. M. Siegel, and D. A. Boas, "Detection of multiply scattered light in optical coherence microscopy," in *Waves and Imaging Through Complex Media*, Chap. 1, part 5, p. 277, Kluwer, New York (2000).
- A. N. Yaroslavsky, P. C. Schulze, I. V. Yaroslavsky, R. Schober, F. Ulrich, H. J. Schwarzmaier, "Optical properties of selected native and coagulated human brain tissues in vitro in the visible and near infrared spectral range," *Phys. Med. Biol.* **47**, 2059–2073 (2002).